



HAL
open science

Numerical exploration of the pitching plate parameter space with application to thrust scaling

Uwe Ehrenstein, Jérémie Labasse, Philippe Meliga

► **To cite this version:**

Uwe Ehrenstein, Jérémie Labasse, Philippe Meliga. Numerical exploration of the pitching plate parameter space with application to thrust scaling. *Applied Ocean Research*, 2020, 101, pp.102278. 10.1016/j.apor.2020.102278 . hal-03235146

HAL Id: hal-03235146

<https://amu.hal.science/hal-03235146>

Submitted on 25 May 2021

HAL is a multi-disciplinary open access archive for the deposit and dissemination of scientific research documents, whether they are published or not. The documents may come from teaching and research institutions in France or abroad, or from public or private research centers.

L'archive ouverte pluridisciplinaire **HAL**, est destinée au dépôt et à la diffusion de documents scientifiques de niveau recherche, publiés ou non, émanant des établissements d'enseignement et de recherche français ou étrangers, des laboratoires publics ou privés.



Distributed under a Creative Commons Attribution - NonCommercial - NoDerivatives 4.0 International License

Numerical exploration of the pitching plate parameter space with application to thrust scaling

Jérémie Labasse^a, Uwe Ehrenstein^{*,a}, Philippe Meliga^b

^a Aix-Marseille Univ, CNRS, Centrale Marseille, M2P2, Marseille, France

^b MINES ParisTech, PSL Research University, Centre de mise en forme des matériaux (CEMEF), CNRS UMR 7635, CS 10207 rue Claude Daunesse, Sophia-Antipolis 06904, France

ARTICLE INFO

Keywords:

Pitching plate

Thrust

Numerical simulation

Laplacian-based mesh moving techniques

ABSTRACT

The thrust performance of a two-dimensional plate pitching harmonically in a uniform flow is assessed numerically using the OpenFOAM toolbox [1]. The mesh displacement vector associated with the rigid body motion is computed as the solution of a Laplace equation with variable diffusivity, using the appropriate mesh manipulation class of the toolbox. For a Reynolds number of 2000, the accuracy of the pressure and viscous stress distributions is assessed by comparison with reference data available for an equivalent fluid configuration. The efficiency and flexibility of the solver allows exploring large ranges of the pitching parameter space, that is the pitching frequency, amplitude and pivot-point location of the pitching plate. The forces induced by the pitching motion are computed for pitching amplitudes up to 15°, for Strouhal numbers varying between 0.2 and 0.5 and for different pitch pivot points. Performing a thrust scaling analysis, a classical theoretical model for the swimming of a waving plate is reliably fitted to the numerical pressure force data. The dependence of the time averaged thrust with the pitching axis is shown to be predicted accurately by a classical potential flow formula (known as Garrick's theory) for pivot points within the front quarter of the plate. The viscous drag is computed as well for the Reynolds number 2000. The time-averaged values are shown to depend on the pitching amplitude and frequency and for instance a Blasius-type scaling, sometimes used to model the viscous drag correction for oscillating two-dimensional foils in this Reynolds number range, is not reliable.

1. Introduction

Unsteady flows past thin oscillating bodies have received considerable attention in the literature. While the objective of early investigations was the understanding and the reduction of undesirable effects of flutter, buffeting and dynamic stall [2], there has been a regain of interest over the last decade, as this type of fluid-structure configurations have applications in connection with the propulsion of flying and aquatic species [3] and the related design of biologically-inspired micro air vehicles. In this context, the wake structure of flapping wings triggered by the generation of vorticity, its shedding, roll-up and subsequent evolution has been the object of numerous investigations. In particular, thrust development on a flapping structure has been explained in terms of the generation of a reversed Kármán vortex-street exhibiting a jet-like average velocity profile, as a result of the shed vortices inducing a velocity in the same direction as the mean flow [4]. It has been recognized, that the wake structure with its mean stream-wise velocity profile can be used to predict the propulsive performance

by applying the integral momentum theorem to a control volume surrounding the body; see, e.g. [5]. This is however somehow questionable because the wake behind a moving foil is highly unsteady, so there is no guarantee that the far field wake velocity remains equal to the free stream velocity (in which case the integrand may not go to zero at the limits of integration), and the velocity fluctuations are likely to be not negligible [6]. More recently, the reliability of the integral momentum approach has been readdressed in [7], comparing PIV measurements with numerical thrust computations for a pitching plate. Direct force measurements aiming at assessing the propulsive performance for oscillating foils are also available (e.g. [8,9]) and more recently for instance in [10,11], just to cite a few.

Scaling laws associated with aquatic locomotion have been reviewed in [12], but they are limited by the fact that thrust is influenced by a large number of parameters, e.g., motion type (heave, pitch, etc.), amplitude, frequency, rigid or flexible surfaces and two-dimensional versus three-dimensional bodies. The Strouhal number has for instance often been adopted as the single parameter of interest for propulsion

* Corresponding author.

E-mail address: uwe.ehrenstein@univ-amu.fr (U. Ehrenstein).

problems involving heaving and/or pitching foils [13]. However, it has been reported that the trailing edge amplitude of motion does influence the thrust generated at a fixed Strouhal number by a heaving foil (as a result of phase differences between forces and motions) but not by a pitching foil [11].

Pitching foils and associated thrust scaling laws have also been addressed numerically, using panel method approaches, for instance in [14] and recently for a finite aspect ratio oscillating plate in [15]. A boundary element method applied to potential flow formulations, together with added mass and circulatory forces modeling, has been applied in [16] to two-dimensional foils with a subsequent generalization to three-dimensional propulsors [17]. Particle vortex method have for instance been used in [18] to predict thrust generation by simulating the wake structure of a flapping foil. A very recent review with a summary on the experimental investigations and numerical methods used to investigate the fluid dynamics of flapping foils can be found in [19].

Despite the important amount of investigations available, there is however no general consensus about analytical models suitable to fit experimental or numerical data. This issue of a reliable thrust scaling is readdressed in the present work using a Navier–Stokes solution procedure for the flow along a pitching plate. Navier–Stokes simulations with a finite element solver have been used for example in [20] to provide thrust coefficients for a pitching airfoil. In [21] a compact finite-difference solution procedure has been employed to scale the thrust and viscous drag of three-dimensional, low-aspect-ratio pitching plates. In this latter work a mapping approach is used to account for the moving boundary, which however puts a bound on the motion’s amplitude in order to prevent numerical instabilities.

For the numerical simulation of a flow in the presence of a moving slender body, one key issue is to couple the body motion with the surrounding flow field via efficient and reliable mesh update methods involving mesh-moving and remeshing. An alternative to mesh updating is to immerse the moving geometry on a simple structured Cartesian grid, but these immersed boundary methods (IBM) [22] require ad-hoc momentum sources to model the relative velocity between the fluid and the solid [23]. It remains challenging to produce accurate force data in the context of vortex-induced propulsion using these methods, because it is difficult to control the accuracy of IBM solutions in the very vicinity of the body surface. This is particularly true for thin bodies-fluid interactions requiring extra care to keep the structure impermeable [24,25].

It is not intended here to review the abundant literature on mesh moving techniques. Some mathematical background for adaptive mesh generation can for instance be found in [26], focusing on mesh-moving algorithms using monitoring functions [27]. Among the mesh update techniques in fluid-structure problems, a popular method for creating a dynamic mesh is to view the fluid grid as an elastic pseudo-structure with large deformations. A pseudo-nonlinear elastostatic equation for the mesh displacement vector has for instance been considered in [28], which is however difficult to solve. A spring analogy of the problem is more tractable, where all point-to-point connections within the mesh are replaced by linear or torsional springs and point motion is obtained as a response to the boundary loading [29–31]. For moderate mesh distortions, linear equations of elasticity under the small deformation assumption are often considered [32,33].

As an alternative to the elasticity analogy, a Laplace equation with variable diffusivity is also used as mesh motion equation. Efficient diffusivity choices are based on the inverse distance from a moving boundary and have been proven efficient to limit mesh distortion in the region close to the moving surface, which reduces the need for local or global remeshing [34,35]. In the present investigation, for the numerical solution procedure the open-source OpenFOAM toolbox is used, that provides a suitable environment for the implementation and rapid dissemination of new algorithms, and has become very popular in academic research [36–40] and industrial flows analysis [41–43]. A

Laplacian-based mesh motion solver has been implemented in OpenFOAM by Jasak and co-workers [44,45]. Here, this dynamic mesh option is used for the simulation of the flow around a pitching plate with vanishing thickness. Benchmark computations, which contribute to the relatively sparse documentation on the use of this mesh update technique, are first performed. For this purpose, pressure and viscous forces acting on the plate are compared with available results [7] for an equivalent flow configuration.

Taking advantage of the solver’s efficiency, the question of the thrust scaling for pitching foils is readdressed and simulations are performed, covering a large parameter range in terms of pitching frequency, angle and pivot point. The numerical data are fitted with a theoretical expression for thrust prediction derived from a potential flow model for waving plates. Comparisons with a classical propulsion law for flapping foils based on potential flow formulas are also performed.

The paper is organized as follows. The numerical model is described in Section 2, together with the various steps which are necessary for the dynamic mesh option in OpenFOAM. In Section 3, pressure and viscous stress results are produced with the toolbox for various pitching regimes and compared to reference experimental and numerical results for validation purposes of the resolution procedure. The thrust scaling is undertaken in Section 4, by exploring numerically the pitching parameter space and a general pressure-thrust scaling law is derived. The scaling results are discussed in Section 5, with regard to finite Reynolds number effects and viscous drag.

2. Numerical model

A plate of length L , pitching with angle amplitude α_0 and frequency f is immersed in an incoming two-dimensional incompressible flow with velocity U_∞ . As in [7] which will be used for validation of the solution procedure, the plate has vanishing thickness. The origin of the fixed Cartesian coordinate system is set at the leading edge of the plate in its horizontal position, with the positive x -axis aligned with the free stream, and positive y -axis in the normal direction. The flow motion is governed by the Navier–Stokes equations

$$\nabla \cdot \mathbf{u} = 0, \quad \rho \frac{\partial \mathbf{u}}{\partial t} + \rho (\mathbf{u} \cdot \nabla) \mathbf{u} = -\nabla p + \mu \nabla^2 \mathbf{u}, \quad (1)$$

where $\mathbf{u} = (u, v)$ is the velocity field and p is the pressure, ρ and μ being the constant density and dynamic viscosity. Uniform flow $(U_\infty, 0)$ is prescribed at inflow and an incoming uniform flow velocity is also the initial condition when starting a new computation. The pitching motion is defined as

$$\theta = \alpha_0 \sin(2\pi f t) \quad \text{and} \quad \left. \begin{aligned} x(t) &= x_0 + (r - r_0) \cos \theta \\ y(t) &= (r - r_0) \sin \theta \end{aligned} \right\} \quad 0 < r < L, \quad (2)$$

where r is the coordinate along the plate, and the coordinate r_0 of the pitch-pivot point corresponds to $(x_0, 0)$ in the fixed coordinate system. In the following, a four-dimensional parameter space is considered, that includes the Reynolds number $\text{Re} = \rho U_\infty L / \mu$, the reduced pitching frequency $k = \pi f L / U_\infty$, the pitching angle α_0 , and the pivot-point position $q = r_0 / L$ relative to the plate length.

Direct numerical simulations of Eq. (1) are performed using the OpenFOAM toolbox version 6 [1]. Since the solver is inherently three-dimensional, only one void cell is used in the z direction to account for the present two-dimensional flow setting. The methodology used in OpenFOAM is based on a finite volume discretization of the differential operators together with a mesh-handling using structured or unstructured grids.

The main features of the discretization, based on Gauss’ theorem applied to the volume integrals, are briefly summarized. For the approximation of the resulting integrals over the control volume

boundaries, the values of the flow quantities at the volume's faces have to be interpolated from the values at the computational nodes. Interpolation practices for finite volume methods are described for instance in [46]. In the forthcoming simulations, for the convective term an upwind interpolation known as upwind differencing scheme is used, where the direction of the flow determines which node provides the cell face value. For the diffusive term a linear interpolation between the faces' two nearest nodes is performed, which is of second order. Linear interpolation is also used for the computation of the gradients normal to the surfaces.

Time discretization is based on the first order implicit Euler scheme. In order to deal with the quadratic non-linearity in the Navier-Stokes system, the equations to be solved at each time step are linearized about the result at the previous time step, in the way that the neglected terms are of second order in time, that is smaller than the error of the time discretization. The time step is adapted during the time integration via the Courant number, well known in computational fluid dynamics. This number is the ratio between the time step and the flow convection time and has been set to 0.9, the characteristic convection time being computed by summing the velocity fluxes and dividing by the cell volume. This yields typical values of order $\Delta t \sim 5 \cdot 10^{-4}$. All linear systems are solved using the built-in *pimpleFoam* predictor-corrector solver, that merges the PISO and SIMPLE algorithms widely used in computational fluid dynamics [46]. The chart for the different options to be set for the pitching-plate case in the OpenFOAM toolbox is provided in Appendix A.

A rectangular computational domain of dimensions $L_x \times L_y$ in the x and y directions is considered, together with open flow boundary conditions consisting of a uniform free-stream $\mathbf{u} = U_\infty \mathbf{e}_x$ at the inflow, free-surface flow conditions $\partial u / \partial y = v = 0$ at the upper and lower boundaries, whereas at the outflow a zero-gradient condition for the velocity field and uniform (zero) pressure is imposed. The meshing procedure in OpenFOAM allows to perform successive refinements. Starting the procedure, a mesh for the outer domain is defined by imposing specific densities m_x and m_y of grid points per unit length on the x and y boundaries of the computational domain, which yields the coarse grid size $(\Delta x, \Delta y) = (L/m_x, L/m_y)$. The mesh is then refined by a factor of 4 via triangulation across a small transient zone, hence an intermediate grid size $(\Delta x/4, \Delta y/4)$ is generated in the subdomain of size $L_{x,s} \times L_{y,s}$ sketched in Fig. 1. Three additional refinements are performed successively in the region adjacent and inside the boundary layer of the plate, as illustrated by the close-up Fig. 2(b). Each refinement is by a factor of 2, hence a fine grid size $(\Delta x/32, \Delta y/32)$ that allows discretizing the boundary layer with $\sim 160 m_y \sqrt{r/L} \text{Re}$ points at a distance r from the leading edge, as obtained from the well-known Blasius boundary layer thickness $\sim 5 \sqrt{rL/\text{Re}}$ [47]. Convergence in the numerical results has been assessed using 5 different meshes exhibiting various spatial extents and grid densities, as detailed in Table 1. Without anticipating on the results, densities $(m_x, m_y) = (22, 25)$ yield 17 boundary-layer grid points at $r = 0.05L$, and 11 points at $r = 0.02L$ (the leading edge is singular for the present case of a plate with vanishing thickness), which we show in the following to be sufficient to resolve accurately the boundary layer.

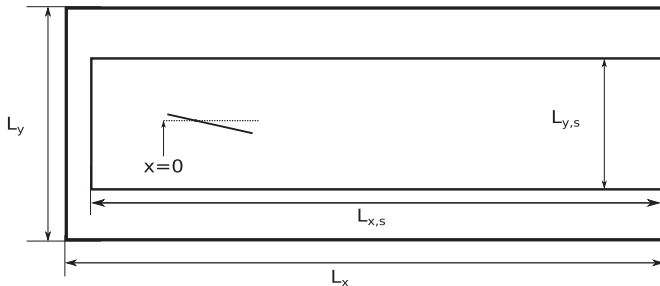


Fig. 1. Sketch of the computational domain.

The OpenFOAM proposes various options to define rigid body motions and in particular for a pitching plate; see [45,48,49] for an overview of the different classes available. We use here the *dynamicFvMesh* class, that applies to cases where the mesh topology does not change (i.e., there is no need to add/remove cells or interfaces). Among the various sub-classes (each of which corresponds to a different mesh motion solver), the focus is on the *dynamicMotionSolverFvMesh* class meant for cases where the mesh points are solved using boundary conditions and diffusivity models. More specifically, we use the *displacementLaplacian* solver that computes the mesh motion from a stationary diffusion equation

$$\nabla \cdot (\gamma \nabla \mathbf{d}) = 0, \quad (3)$$

where γ is a diffusivity coefficient and \mathbf{d} is the mesh displacement vector needed to update the mesh, computed as the solution of a Dirichlet-type boundary value problem. Within the *displacementLaplacian* class, the *pointVectorField* class allows defining certain types of rigid body motions, in particular the *angularOscillatingDisplacement* type that corresponds to a pure pitching motion, whose frequency, amplitude and pivot-point can be user-defined. When performing the time-stepping in the simulation procedure, the Navier-Stokes and Laplace equations are solved in a sequential fashion, with the diffusivity coefficient set proportional to the inverse of some measure of the distance to the moving boundary to ensure minimal distortion (*inverseDistance* option). Again, the reader interested in more practical details regarding the implementation of the *displacementLaplacian* solver is referred to Appendix A.

3. Benchmark results

This section reports reference data for pitching plate investigations in the range of reduced frequencies $k < 5$. The Reynolds number is set to $\text{Re} = 2000$, the pitching angle to $\alpha_0 = 10^\circ$, and the pitch-pivot point is at $q = 1/3$, so as to match the configuration studied experimentally and numerically in [7]. In this latter work an experimental investigation has been performed for a three-dimensional plate of span $4.7L$, large enough for the flow along the center region of the plate to be quasi-two-dimensional, and of thickness $0.075L$, small enough to avoid body-shape effects during the pitching motion. The measurements match remarkably well the numerical results obtained by the same authors for a two-dimensional plate with vanishing thickness, using a high-order (8th order) compact finite differences discretization [50], together with a multi-domain approach (details about this numerical approach are provided in [51]). Given the completely different numerical solution procedures, the reliability of the OpenFOAM computations, at least for the problem under investigation, can hence be assessed by comparing the present results with those reported in [7]. In particular, the mesh-convergence is only assessed via comparison of the results at different discretization levels, contrary to mathematically rigorous convergence analyses as proposed for instance in [52].

The comparison focuses here on the x -component of the (dimensionless) time-averaged pressure and viscous stresses distribution over the plate, that is

$$\langle f_p^* \rangle = -\frac{1}{\rho U_\infty^2} \frac{1}{T} \int_{t_0}^{t_0+T} (-p) n_x \, dt, \quad (4)$$

$$\langle f_\mu^* \rangle = -\frac{1}{\rho U_\infty^2} \frac{1}{T} \int_{t_0}^{t_0+T} \mu \left(2 \frac{\partial u}{\partial x} n_x + \left(\frac{\partial u}{\partial y} + \frac{\partial v}{\partial y} \right) n_y \right) dt, \quad (5)$$

where dimensionless quantities are written with an asterisk, the brackets $\langle \cdot \rangle$ denote the average over time, n_x and n_y are the x - and y -components of the outward unit vector normal to the plate. Note that the minus sign is applied for a positive total force to correspond to thrust on the plate, which is the convention generally used. The pressure in (4) is the computed pressure shifted by a constant in order to be zero at the inflow.

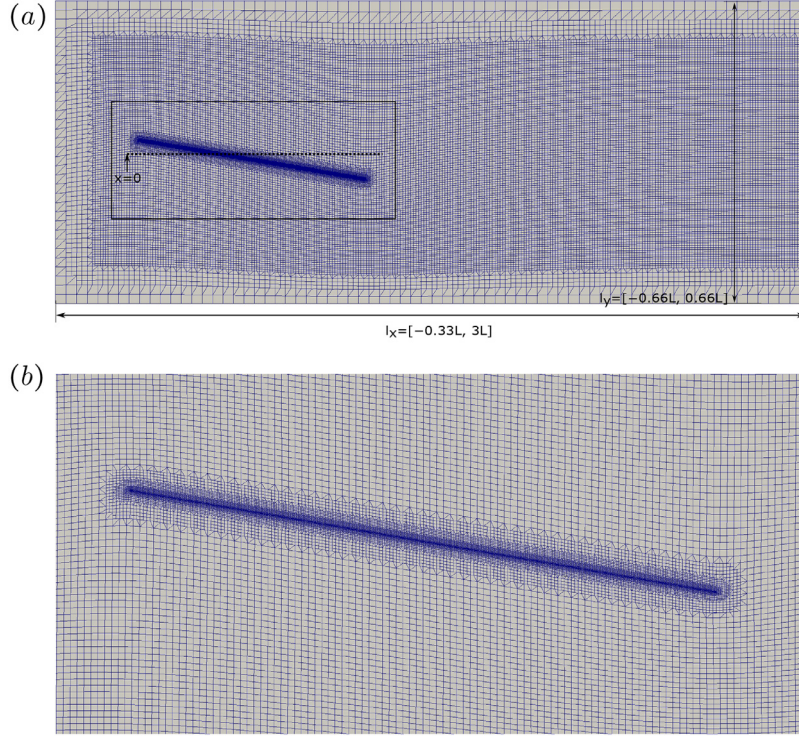


Fig. 2. Example of the mesh structure, (a) in a subdomain $l_x \times l_y$ of the computational domain $L_x \times L_y$ (cf. Table 1); (b) zoom near the plate corresponding to the rectangle drawn in (a).

In practice, the initial condition drives a transient regime that lasts over 6 to 10 pitching periods (depending on the case considered), before the flow eventually reaches a time-periodic, vortex-shedding state, as illustrated in Fig. 3 by the instantaneous snapshot of the vorticity contours computed along the plate and in the wake for a pitching frequency $k = 3.8$. In the benchmark computations discussed hereafter, all time-averaged quantities are computed using a simple trapezoidal rule, discretizing one period of the plate motion into at least 64 (and up to 128) equidistant snapshots after the periodic regime has been reached.

We assess first the relevance of the numerical approach by comparing the results obtained with meshes M_1 and M_1^+ for identical plate position with respect to the inflow, outflow and lateral boundaries as used for the computations in [7]. As seen from Table 1, the difference is in the grid refinement, as M_1 has densities $(m_x, m_y) = (22, 25)$ points per unit length (hence fine grid sizes $0.0014L$ and $0.0012L$ in the x - and y - directions, respectively) while M_1^+ is generated with twice as many grid points in each direction (cf. the values in Table 1).

The pressure and viscous stress results are shown in Fig. 4 for three reduced frequencies $k = 2.5$, 3.8 and $k = 5$ and are seen to be almost identical, which confirms that the M_1 grid is sufficient to accurately resolve the flow around the plate. There is also a very good agreement with the results of [7] shown as well (the region $r/L < 0.1$ is omitted in these results, because the authors use a coordinate transformation to map the physical coordinates into computational ones, which makes it

difficult to handle the leading edge singularity for this case of plate with vanishing thickness). This overall agreement of the pressure and viscous stresses is remarkable given the completely different resolution procedures, and gives confidence that the present numerical approach is sound. In [7], the plate's motion is given by a simplified pitching function

$$y = (x - x_0)\alpha_0 \sin(2\pi ft), \quad (6)$$

that can be seen as a leading-order approximation of (2) in the limit where $\alpha_0 \ll 1$ (in which case $\cos \theta \equiv 1$ and $\sin \theta \equiv \theta$). This is likely to explain the observed limited discrepancies along the plate, especially in terms of the viscous stress distribution close to the leading edge. Also, in the function (6) the leading and trailing edges have fixed x -coordinates, which can be interpreted as a small numerical stretching of the plate length, that takes the value $L\sqrt{1 + \tan^2 \alpha_0}$ in the plate maximal peak position. For the pitching angle $\alpha_0 = 10^\circ$ considered herein, the stretching is by $\sim 1.5\%$.

Before addressing the thrust scaling issue in the next section, the influence of the spatial extent of the computational domain on the computed mean force distribution is briefly examined. For this purpose, four meshes M_1 , M_2 , M_3 and M_4 are built with the same densities $(m_x, m_y) = (22, 25)$, the different mesh parameters being listed in Table 1. For the meshes M_1, M_2, M_3 , the outflow boundary is kept at the same distance $3.33L$ from the plate's trailing edge, but the distance

Table 1
Mesh parameters for the computational domain sketched in Fig. 1.

	M_1	M_1^+	M_2	M_3	M_4
L_x	$[-0.33L, 4.33L]$	$[-0.33L, 4.33L]$	$[-0.66L, 4.33L]$	$[-1L, 4.33L]$	$[-0.66L, 6L]$
L_y	$[-0.66L, 0.66L]$	$[-0.66L, 0.66L]$	$[-L, L]$	$[-1.5L, 1.5L]$	$[-L, L]$
$L_{x,s}$	$[-0.16L, 4.33L]$	$[-0.16L, 4.33L]$	$[-0.33L, 4.33L]$	$[-0.66L, 4.33L]$	$[-0.33L, 6L]$
$L_{y,s}$	$[-0.5L, 0.5L]$	$[-0.5L, 0.5L]$	$[-0.66L, 0.66L]$	$[-1.33L, 1.33L]$	$[-0.66L, 0.66L]$
m_x	22	44	22	22	22
m_y	25	50	25	25	25

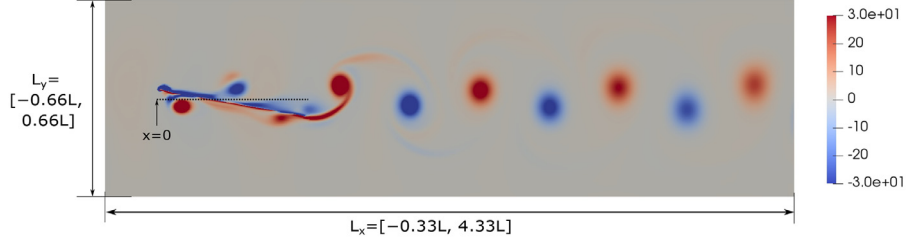


Fig. 3. Instantaneous snapshot of the (dimensionless) vorticity contours in the computational domain $L_x \times L_y$ (cf. [Table 1](#)) for a Reynolds number $Re = 2000$, a reduced frequency $k = 3.8$, a pitching angle $\alpha_0 = 10^\circ$ and a pitch-pivot point located at $q = 1/3$.

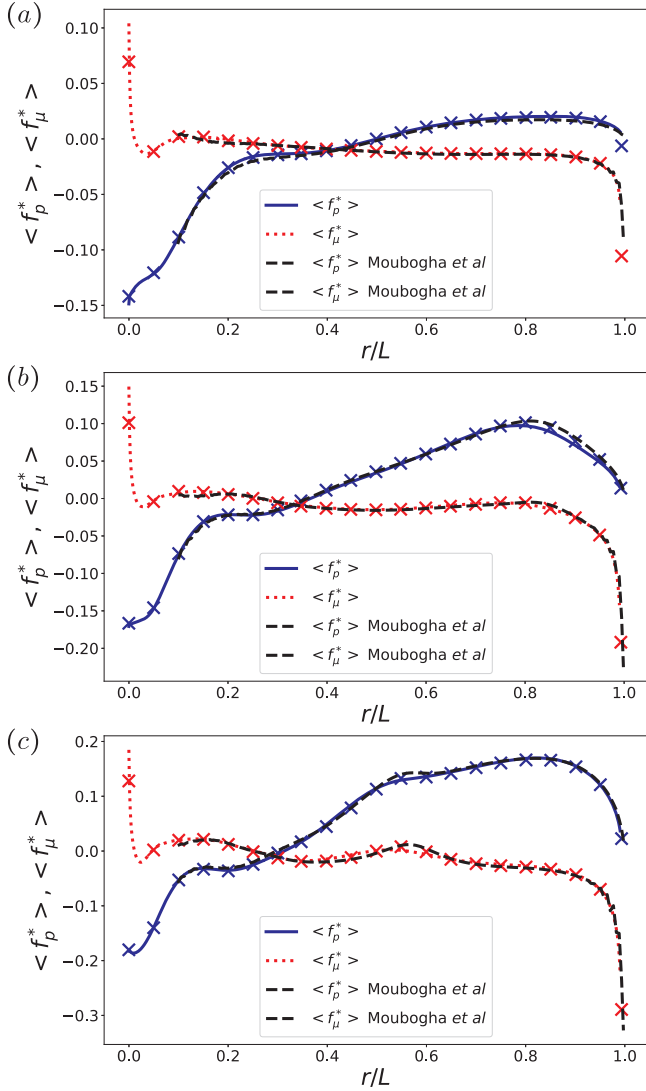


Fig. 4. Dimensionless mean pressure stress $\langle f_p^* \rangle$ and viscous stress $\langle f_\mu^* \rangle$, computed along the plate's upper face as function of the distance r/L from the leading edge, at the reduced frequency (a) $k = 2.5$, (b) $k = 3.8$ and (c) $k = 5$. For all three plots, the Reynolds number is $Re = 2000$, the pitching angle is $\alpha_0 = 10^\circ$ and the pitch-pivot point is located at $q = 1/3$. Results corresponding to mesh M_1 (resp. mesh M_1^+) are represented as the colored lines (resp. symbols \times). The reference results of [7] are superimposed as the black lines.

between the inflow and the plate's leading edge is increased from $0.33L$ to L , whereas the distance between the lateral boundaries is increased from $4L/3$ to $3L$. The results obtained only for the highest reduced frequency $k = 5$ are provided in [Fig. 5](#), the tendencies being the same for the other pitching frequencies. We observe small but non-negligible discrepancies between M_1 and M_2 , meaning that the M_1 results are not

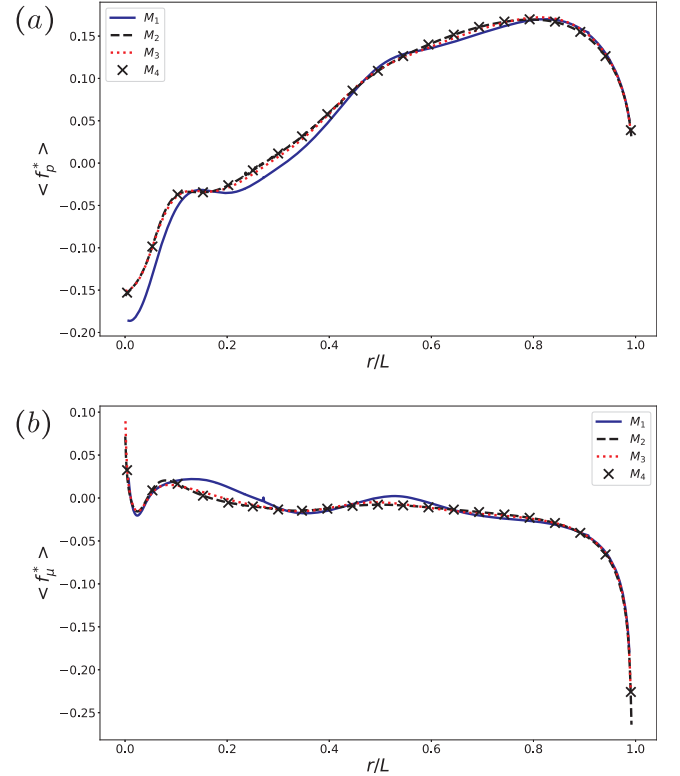


Fig. 5. Dimensionless mean (a) pressure stress $\langle f_p^* \rangle$ and (b) viscous stress $\langle f_\mu^* \rangle$, computed along the plate's upper face $0 < r/L < 1$, at the reduced frequency $k = 5$, for a Reynolds number $Re = 2000$, a pitching angle $\alpha_0 = 10^\circ$ and a pitch-pivot point located at $q = 1/3$. Results corresponding to meshes M_1 , M_2 and M_3 are shown as the solid blue, black dashed, and red dotted lines, respectively. The result for mesh M_4 is depicted by the symbol \times . (For interpretation of the references to colour in this figure legend, the reader is referred to the web version of this article.)

entirely free from finite size effects (a conclusion already briefly drawn in [7], although the authors did not report a convergence study). In contrast, a near-perfect agreement is obtained between M_2 and M_3 . The influence of the outflow boundary remains to assess and in mesh M_4 , its distance from the plate's trailing edge has been increased to $5L$, the other parameters being those from M_2 . The result is shown in [Fig. 5](#) as the symbol \times and there is again an agreement with the M_2 computations, which justifies retaining M_2 as the reference set-up from now on.

As mentioned before, for the benchmark comparisons the time-averaging has been performed over one pitching period (once a periodic regime reached), as in [7]. A thrust scaling analysis is undertaken in the next section, by varying the pitching angle, the pitching frequency and the pitch-pivot point location. There is however no guarantee, in particular for large pitching angles and frequencies, that an exact periodic regime of the flow state is reached after the transient phase. The time evolution of the thrust $\frac{1}{L} \oint f_p^* dr$ (with $f_p^* = (-p)n_x$ the pressure stress)

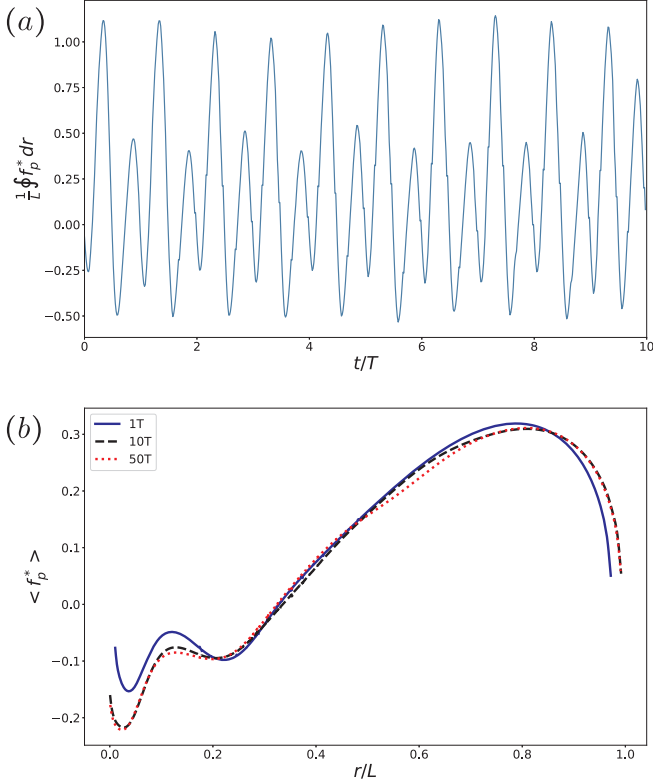


Fig. 6. Temporal evolution (a) of the integrated pressure stress $\frac{1}{L} \oint f_p^* dr$ and (b) the time-average (f_p^*) of the pressure stress along the plate's upper face $0 < r/L < 1$ using 1, 10 and 50 pitching cycles, at the reduced frequency $k = 9$, pitching angle $\alpha_0 = 15^\circ$ and pitch-pivot point at $q = 1/3$. The Reynolds number is $Re = 2000$ and the M_2 mesh has been used.

for the highest pitching angle $\alpha_0 = 15^\circ$ which will be considered in the next section is shown in Fig. 6(a) over 10 pitching periods, once the flow has settled down. For this example, the pitch-point location is $q = 1/3$, and the reduced frequency $k = 9$ is high.

It is seen that indeed the time-signal is only approximately periodic with respect to the pitching period T and one observes a small global undulation. The mean pressure-stress along the plate's upper face is shown in Fig. 6(b), considering 1, 10 and 50 pitching cycles, respectively, for the time-averaging procedure (with 70 equidistant snapshots for one period). It is seen that besides differences of the mean stress near the leading edge $r = 0$, the results are very close, whatever number of cycles is considered. For instance, when averaging the signal in Fig. 6(a) for the first period T shown one gets a value 0.2180, whereas the mean value for an interval of $10T$ gives 0.2025 and for $50T$ one gets 0.2042, that is the difference is only about 6%. For the thrust analysis discussed in the next section, the time-averaging has therefore been performed over one pitching period, having verified also for other parameter configurations, that a time-averaging over more than one cycle (of course beyond the transient regime) has only a marginal effect on the thrust prediction.

4. Thrust scaling

The reliability of the numerical solution procedure having been assessed in the previous section, a parameter exploration for the pitching plate is performed in view of a thrust scaling analysis. During the pitching motion, the force exerted by the fluid on the plate has an inertial reactive component, owing to the fluid accelerated by the body motion. The inertial resistive force, that is the form drag, is zero for the present zero-thickness plate and only the skin friction drag opposes the thrust force.

For potential flow and in the limit of small pitching angles, the reaction of the fluid accelerated by the body has been formulated in [53], and the theoretical model of the induced local force (per unit span in the present two-dimensional setting) reads (see also [54–56])

$$\mathbf{f}_{p,th}(r, t) = -\mathcal{M} \left(\frac{\partial}{\partial t} + U_\infty \frac{\partial}{\partial r} \right)^2 y(r, t) \mathbf{n}, \quad (7)$$

with \mathcal{M} the added-mass coefficient and

$$\mathbf{n} = \pm(-\sin \theta, \cos \theta), \quad (8)$$

the unit normal vector at the plate (with plus sign for the upper face of the plate and minus sign for the lower face, consistently with the convention used in Section 3). It is well known [57] that the added mass per unit span of a plate with length L and moving normal to its surface is equal to $\pi \rho L^2/4$ which corresponds to

$$\mathcal{M} = \frac{\pi}{4} \rho L, \quad (9)$$

in the local force expression (7).

Substituting (2) for the y pitching displacement and (8) for the normal vector \mathbf{n} in (7), projecting in the negative streamwise x direction (for the thrust coefficient to be positive) and integrating along the plate yields the following expression for the dimensionless theoretical pressure thrust

$$\begin{aligned} F_{p,th}^* &= -\frac{1}{\rho U_\infty^2 L} \frac{1}{T} \int_0^T \oint \mathbf{f}_{th}(r, t) \cdot \mathbf{e}_x dr dt, \\ &= \frac{\pi((L-r_0)^2 - r_0^2)}{4U_\infty^2} (\langle (\dot{\theta} \sin \theta)^2 \rangle - \langle \ddot{\theta} \cos \theta \sin \theta \rangle) \\ &\quad - \frac{\pi L}{U_\infty} \langle \dot{\theta} \cos \theta \sin \theta \rangle, \end{aligned} \quad (10)$$

where we denote by $\dot{\theta}$ the time derivative of the time-dependent pitching angle. In the limit of small pitching angles, the term quadratic in the angular velocity $\langle (\dot{\theta} \sin \theta)^2 \rangle$ is of order α_0^4 and is thus negligible in comparison to the other two terms of order α_0^2 , hence, given that $q = r_0/L$,

$$F_{p,th}^* = -\frac{\pi L^2}{4U_\infty^2} (1-2q) \langle \dot{\theta} \cos \theta \sin \theta \rangle - \frac{\pi L}{U_\infty} \langle \dot{\theta} \cos \theta \sin \theta \rangle. \quad (12)$$

This expression can be written equivalently

$$F_{p,th}^* = C_1 \frac{\pi L^2}{4U_\infty^2} (1-2q) \alpha_0^2 4\pi^2 f^2 + C_2 \frac{\pi L}{U_\infty} \alpha_0^2 2\pi f, \quad (13)$$

with

$$C_1 = -\frac{\langle \dot{\theta} \cos \theta \sin \theta \rangle}{\alpha_0^2 4\pi^2 f^2} \quad C_2 = -\frac{\langle \dot{\theta} \cos \theta \sin \theta \rangle}{\alpha_0^2 2\pi f}, \quad (14)$$

allowing to write the thrust formula in terms of the reduced pitching frequency as

$$F_{p,th}^* = C_1 \pi (1-2q) \alpha_0^2 k^2 + 2C_2 \pi \alpha_0^2 k. \quad (15)$$

Equivalently, this formula can be expressed in terms of the Strouhal number $St = Af/U_\infty$, where $A = 2(1-q)L \sin \alpha_0$ is the trailing edge peak-to-peak amplitude of motion. Since the small-pitching-angle assumption underlies the derivation of formula (13), this gives

$$St = \frac{2}{\pi} (1-q) k \sin \alpha_0 \sim \frac{2}{\pi} (1-q) k \alpha_0 \quad (16)$$

and thus

$$F_{p,th}^* = C_1 \frac{\pi^3}{4} \frac{1-2q}{(1-q)^2} St^2 + C_2 \pi^2 \frac{1}{1-q} St \alpha_0. \quad (17)$$

An expression similar to (17) has been proposed for instance in [11] and generalized in [21] to finite-aspect-ratio pitching plates. In practice, the ideal values for C_1 and C_2 , obtained retaining only the leading-

order terms of $\cos \theta$ and $\sin \theta$ are

$$C_1 = \langle \sin^2(2\pi f) \rangle = \frac{1}{2}, \quad C_2 = -\langle \sin(2\pi f) \cos(2\pi f) \rangle = 0. \quad (18)$$

It is however unclear whether these theoretical values when used in relations (15)–(17) fit actual experimental or numerical results. Several recent studies derive a model equivalent to (17) setting $C_2 = 0$; see, e.g. the experimental investigation reported in [11]. It has however been argued that there is no reason to set C_1 and C_2 equal to the ideal values, because the fluid-plate dynamics is likely to introduce phase shifts between the periodic wall displacement and the induced fluid velocity and acceleration.

In order to shed new light on this issue, 35 computations have been performed by varying the pitching angle α_0 , from 5° up to 15° by increments of 2.5° and the Strouhal number from 0.2 up to 0.5 by increments of 0.05, with the Reynolds number remaining $Re = 2000$ and the pitch-pivot point now at the leading edge ($q = 0$). The small pitching angle approximation is expected to hold, since $\max\{\alpha_0\} = 0.26$, meaning that the difference between $\sin \alpha_0$ and α_0 is at most 1.1%. For every set of parameters, the simulations have been performed until a periodic regime is achieved. The dimensionless pressure stress has been integrated along the plate. In Fig. 7, the resulting dimensionless pressure force

$$F_p^* = \frac{1}{L} \oint \langle f_p^* \rangle dr, \quad (19)$$

is plotted as a function of the Strouhal number, with each symbol corresponding to a different pitching angle. We observe that the thrust force does not depend on St alone, but that the angle α_0 , although entering in the definition of St , is to be considered as an independent parameter. Note in particular that for a given Strouhal number, the thrust diminishes with increasing angle, meaning that the coefficient C_2 in (17) must be non zero and negative in order to fit the results with the theoretical formula.

This is confirmed by a conventional least-square fit which provides the coefficients C_1, C_2 in the scaling formula (17), such that the residual

$$\sum_j ((F_p^*)_j - (F_{p,th}^*)_j)^2, \quad (20)$$

is minimal, where $j = 1, 2, \dots$ labels the 35 thrust samples obtained in the (α_0-St) parameter space (7 Strouhal numbers and 5 pitching angles).

The least-square procedure yields $C_1 = 0.332$, $C_2 = -0.225$, for which the numerical results exhibit an excellent agreement with the theoretical pressure thrust $F_{p,th}^*$ shown as the horizontal axis in Fig. 8. We recall that, according to the assumptions underlying the derivation of the model (15)–(17), C_1 is related to the time average between the

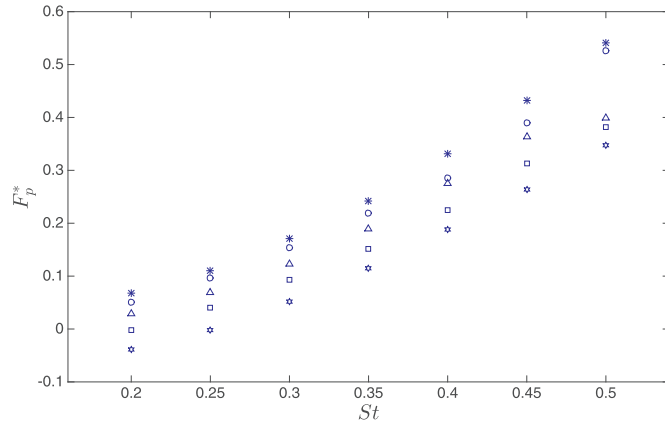


Fig. 7. Computed time-averaged thrust F_p^* as function of the Strouhal number, as obtained for pitching angles $\alpha_0 = 5^\circ$ (*), $\alpha_0 = 7.5^\circ$ (○), $\alpha_0 = 10^\circ$ (△), $\alpha_0 = 12.5^\circ$ (□), $\alpha_0 = 15^\circ$ (☆) at Reynolds number $Re = 2000$, with a pitch-pivot point at the leading edge ($q = 0$).

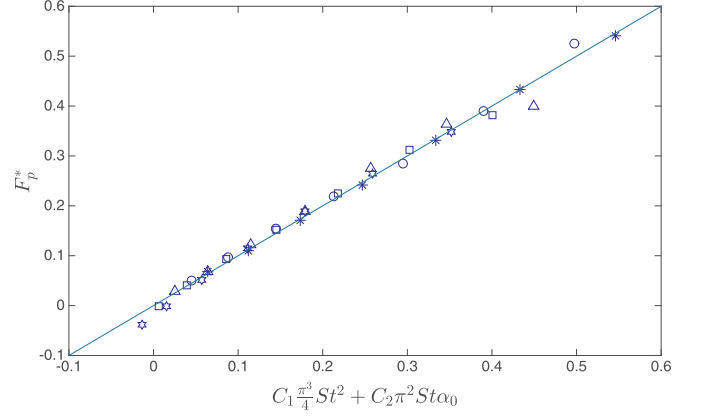


Fig. 8. Computed time-averaged thrust F_p^* against its theoretical counterpart $F_{p,th}^*$ computed from model (17) with $C_1 = 0.33$ and $C_2 = -0.22$. The various symbols represent 35 data points obtained in the (α_0-St) parameter space, by considering 7 Strouhal numbers $0.2 \leq St \leq 0.5$, and 5 pitching angles $\alpha_0 = 5^\circ$ (*), $\alpha_0 = 7.5^\circ$ (○), $\alpha_0 = 10^\circ$ (△), $\alpha_0 = 12.5^\circ$ (□), $\alpha_0 = 15^\circ$ (☆), for the Reynolds number $Re = 2000$, and a pitch-pivot point at the leading edge ($q = 0$); see Fig. 7. The solid line corresponds to the bisector of the first quadrant angle.

displacement and acceleration term, whereas C_2 comes from the time-average between displacement and velocity. Interestingly, the fitted values are in the interval $[-0.5, 0.5]$, but they are different from the idealized values (0.5 and 0 respectively), highlighting the existence of phase shifts between displacement, velocity and acceleration in the present fluid-structure dynamics.

For the same pitching angles and Strouhal numbers as considered above, the procedure has been repeated by varying the pitch-pivot position q which also enters the scaling formulas (15)–(17). Concerning aquatic motion, the Strouhal number (16) formed with the tail beat-amplitude is the appropriate parameter (and it is in the range of 0.2 to 0.5 for diverse species of fish and cetaceans [58]). For the trailing-edge excursion to be dominant over the leading-edge excursion during pitching, pitch-pivot point locations have been chosen in the range $0 \leq q \leq 0.4$ and for the complete parameter space (St, α_0, q) considered, the reduced frequency is in the range $1 < k < 15$ according to (16).

For each value of q , it is convenient to report in Fig. 9 the computed

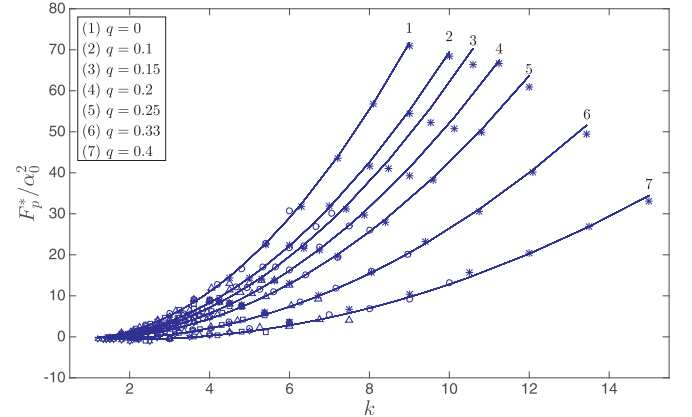


Fig. 9. Computed time-averaged thrust F_p^*/α_0^2 as function of the reduced frequency k . Seven different positions q of the pitch-pivot point have been considered, as indicated by the labels. For each label, the various symbols again represent the 35 data points obtained at $Re = 2000$ in the (α_0-k) parameter space for the same 7 Strouhal numbers $0.2 \leq St \leq 0.5$ and 5 pitching angles $5^\circ \leq \alpha_0 \leq 15^\circ$ as in figure 7. The solid curves correspond to theoretical thrust $F_{p,th}^*/\alpha_0^2$ computed from model (15), with C_1 and C_2 coefficients (shown in Fig. 10) optimized for each value of q through a least-square procedure.

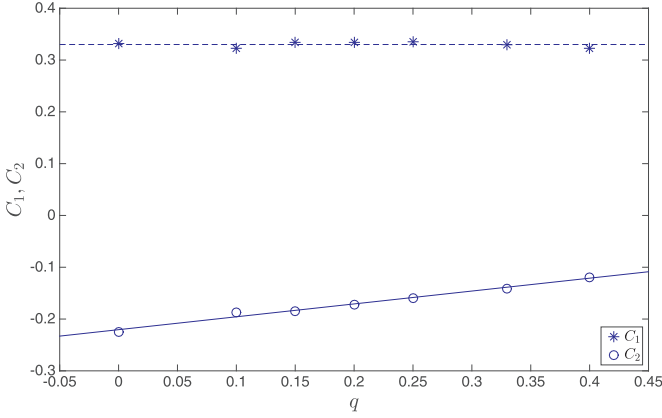


Fig. 10. Coefficients C_1 and C_2 as function of the pitch-point position q for the least-square fit between (17) and the computed time-averaged thrust (19). For each value of q , the same Strouhal numbers $0.2 \leq St \leq 0.5$ and pitching angles $5^\circ \leq \alpha_0 \leq 15^\circ$ as in figure 7 have been considered. The broken line corresponds to $C_1 = 0.33$ and the solid line to $C_2(q) = -0.22 + 0.25q$.

thrust values divided by α_0^2 , i.e., F_p^*/α_0^2 , as those should be close to a second order polynomial in k , according to (15). Similar to Fig. 7, each symbol in Fig. 9 indicates a given pitching angle, while the reduced frequency k corresponds to a given Strouhal number according to (16). For each pitch-pivot position, the F_p^*/α_0^2 data are seen to evolve along distinct and separate curves, which is in agreement with (15). Also, the thrust decreases for increasing distance of the pivot-point from the leading edge, which is in qualitative agreement with experimental observations reported for instance in [59]. The solid lines in Fig. 9 correspond to the theoretical formula $F_{p,th}^*/\alpha_0^2$ obtained from (15), whose C_1 and C_2 have been computed repeatedly for each pivot-point location from a least-square fit over the 35 thrust samples obtained in the (α_0-k) parameter space. The obtained coefficients are reported in Fig. 10, where one observes that the C_2 coefficient varies quite significantly with the pitch-pivot position, while the coefficient C_1 remains approximately constant. As mentioned before, the C_2 value is triggered by the existence of phase shifts between the periodic wall displacement and the induced fluid velocity and acceleration. The variation of C_2 is hence not too surprising, because there is no reason that such phase shifts should remain identical over the whole parameter space, and in particular over the whole range of pitch-pivot-point locations.

As can be seen in Fig. 10, the C_2 values vary almost linearly with q and a simple fit gives

$$C_1 = 0.33, \quad C_2(q) = -0.22 + 0.25q. \quad (21)$$

Using these values in the formula (17), the Fig. 11 shows that the 245 samples (for the 7 pitch-pivot configurations, the 7 Strouhal numbers and 5 pitching angles considered) match closely the theoretical prediction shown as the horizontal axis.

It is recalled that this prediction relies on the theoretical model (7) for the reaction of the fluid accelerated by the plate's motion derived in [53]. In [16], time-averaged thrust forces for a pitching airfoil have been compared with Garrick's theory [60] based on potential flow formulas derived in [61], for an idealized airfoil represented as a straight line. The time-averaged value of the propelling force P_x is given in [60], which also applies to variable pitch-pivot point positions. It takes the following dimensionless expression with the present notations for the pitching plate

$$\langle P_x^* \rangle = \frac{\pi k^2 \alpha_0^2}{2} \left[\left(\frac{3}{2} - 2q \right) \left(\frac{1}{2} - F \right) + \left(\frac{1}{2} - 2q \right) \frac{G}{k} - \frac{F}{k^2} + (F^2 + G^2) \left(\frac{1}{k^2} + \left(\frac{3}{2} - 2q \right)^2 \right) \right], \quad (22)$$

F and G being function of the reduced frequency k involving Bessel

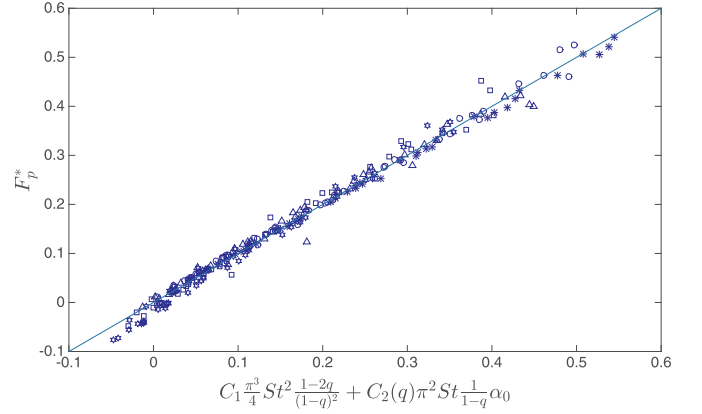


Fig. 11. Computed time-averaged thrust F_p^* against its theoretical counterpart $F_{p,th}^*$ computed from model (17) with $C_1 = 0.33$ and $C_2(q) = -0.22 + 0.25q$ using the full set of parameters (pitch-point position $0 \leq q \leq 0.4$, Strouhal number $0.2 \leq St \leq 0.5$, pitching angle $5^\circ \leq \alpha_0 \leq 15^\circ$), together with Reynolds number $Re = 2000$. The solid line corresponds to the bisector of the first quadrant angle.

functions of the first and second kind given in [60]. The above formula (with $q = 0$) has been shown in [16] to predict quite accurately the thrust force and it has also been used for comparison with numerical computations for a NACA airfoil with a pitch-pivot point at one quarter chord in [14]. The effect of pivot axis location, including configurations with pivot points ahead or downstream the airfoil, have also been addressed experimentally in [10] and compared with Garrick's linear theory. This scaling is compared in Fig. 12 with the scaling $F_{p,th}^*$ using the parameter values (21) in (15), for $q = 0, 0.2, 0.4$ and the different pitching angles considered. It is seen, that for $q = 0$ and $q = 0.2$, Garrick's scaling is rather close to the prediction $F_{p,th}^*$ and in particular for higher k -values (the results only up to $k = 8$ are shown, in order to better distinguish the differences for lower frequencies). For the pitch-pivot point $q = 0.4$ Garrick's curve however overpredicts the thrust.

The values of F and G in (22) are tabulated in [60] and are shown to converge for increasing k towards 0.5 and 0, respectively. This yields the asymptotic expression (setting $F = 0.5, G = 0, F/k^2 = 0$ in (22))

$$\langle P_x^* \rangle \sim \pi k^2 \alpha_0^2 \left(\frac{9}{32} - \frac{3q}{4} + \frac{q^2}{2} \right). \quad (23)$$

For instance, it can be checked that for $k \geq 3$ this simplified formula differs only about few percent from (22), when varying q from 0 to 0.4. Using the expressions (21) for C_1 and $C_2(q)$ in (15), this formula

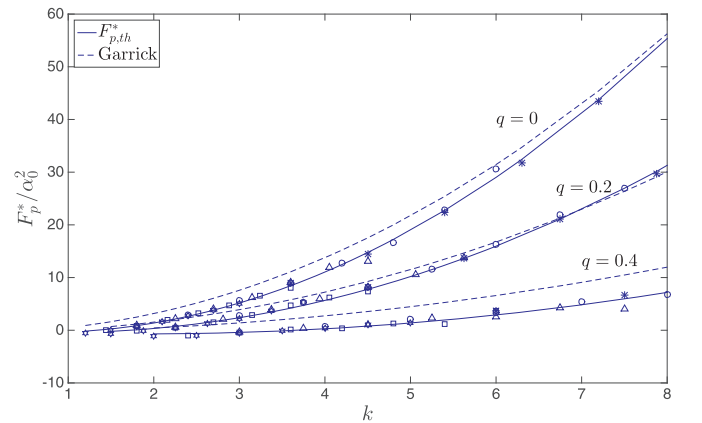


Fig. 12. Computed time-averaged thrust F_p^*/α_0^2 as function of the reduced frequency k , against its theoretical prediction $F_{p,th}^*$ given by (15) with $C_1 = 0.33$, $C_2(q) = -0.22 + 0.25q$ and compared with Garrick's prediction (22), for three different pitch-pivot point positions $q = 0, 0.2, 0.4$. The symbols for the pitching angles $5^\circ \leq \alpha_0 \leq 15^\circ$ are the same as in Fig. 7.

becomes

$$F_{p,th}^* = \pi\alpha_0^2 [0.33 k^2 - 0.44 k - q (0.66 k^2 - 0.5 k)]. \quad (24)$$

For large k -values the k^2 terms dominate and it is seen when comparing with (23), that for $q < 0.2$ the predictions are indeed close to Garrick's theory.

The dependence of $C_2(q)$ on q has been inferred from the results up to $q = 0.4$ and extrapolating to $q = 0.5$ would give according to (24) a negative thrust $F_{p,th}^* - 0.19\pi\alpha_0^2 k$ decreasing linearly with k . To verify if this trend is retrieved in the computations, some simulations have been performed with $q = 0.5$ and indeed the thrust values proved to be negative. For instance, for $\alpha_0 = 5^\circ$ and $St = 0.2$ (that is $k = 7.2$), one finds $F_p^* = -0.028$ and at $\alpha_0 = 15^\circ$ and $St = 0.4$ (that is $k = 4.8$) one gets $F_p^* = -0.160$. The extrapolation would give the values -0.032 and -0.186 which compare fairly well. Garrick's formula however predicts thrust which is still positive for $q = 0.5$ which shows the limit of a possible comparison with potential flow theory.

Garrick's general formula is rather complicated, while the scaling formula $F_{p,th}^*$ proposed here can easily be derived from the theoretical expression (7) and it can easily be written in terms of the reduced frequency or the Strouhal number. It has however to be emphasized that while the parameter C_1 in (15) appears to be independent of the pitch-pivot point location q , a linear function $C_2(q)$ proved necessary for a reliable scaling.

5. Concluding remarks

The present numerical investigation has shown that the combination of an easy-to-use Laplacian-based dynamic mesh procedure and the physical modelling capabilities of OpenFOAM provides a powerful numerical framework, particularly suitable for flow computations along rigid objects moving with prescribed archetypal motions, like the pitching motion considered here. Beyond the reported accuracy, the solver is also efficient. Indeed, the running time needed to ensure convergence of the mean force distributions with the M_2 mesh (that is 1.5×10^5 grid points; see Table 1) is about 50 min using 16 cores (Dell PowerEdge C6420) on the HPC cluster of Aix-Marseille Université. An extensive parameter investigation could therefore be performed, with 245 simulations spanning 7 oscillation frequencies, 5 pitching angles, and 7 pivot-point position. The propulsive performance has been systematically and reliably assessed, and a thrust analytical model (17) has been successfully fitted with the generated data set. This thrust model could easily be derived and its expression is a fairly simple function of the three pitching parameters.

One key approximation underlying the latter thrust scaling is the purely potential formulation needed to estimate the theoretical pressure thrust (7), while all results so far have been obtained for the finite Reynolds number $Re = 2000$. Additional simulations have been performed at $Re = 1000$ and $Re = 3000$ to assess the sensitivity of the pressure stress to finite Reynolds number effects. The results obtained for a reduced frequency $k = 5$, pitching angle $\alpha_0 = 10^\circ$ and pitch-pivot point at $q = 1/3$ are shown in Fig. 13, where the pressure stress distribution is seen to remain the same, regardless of the value of the Reynolds number. This gives confidence that the present pitching thrust scaling has some general significance when viscous flow is considered, at least for values of Re above a certain threshold.

In concluding this study, the viscous drag along the moving plate is also addressed, as it opposes the thrust generated by the pressure stress at a finite Reynolds number (the form drag is zero in the present case of a zero-thickness plate), meaning that the true propulsive performance of the pitching plate does not solely depend on the scaling laws discussed in the previous section. In an attempt to quantify the viscous drag, the mean viscous stress distribution $\langle f_\mu^* \rangle$ computed at $Re = 2000$ has been integrated along the plate. It is recalled that the convergence of this flow quantity has been assessed in Section 3 (see Fig. 4). In Fig. 14, the resulting dimensionless viscous drag force

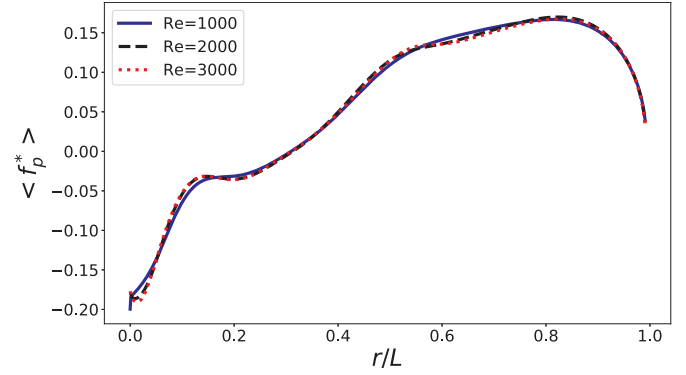


Fig. 13. Dimensionless mean pressure stress $\langle f_p^* \rangle$ computed along the plate upper face as function of the distance r/L from the leading edge for a reduced frequency $k = 5$, a pitching angle is $\alpha_0 = 10^\circ$ and a pitch-pivot position $q = 1/3$ at $Re = 1000$ (—), $Re = 2000$ (- -) and $Re = 3000$.

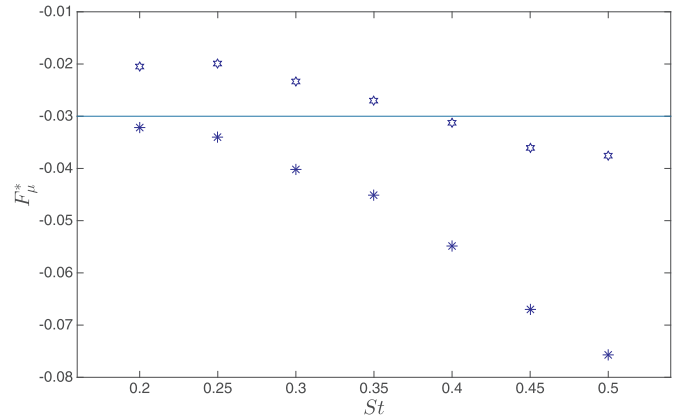


Fig. 14. Computed time-averaged viscous drag F_μ^* as function of the Strouhal number, for pitching angles $\alpha_0 = 5^\circ$ (*) and $\alpha_0 = 15^\circ$ (☆), together with a Reynolds number $Re = 2000$, and a pitch-pivot point at the leading edge ($q = 0$). The straight line corresponds to the Blasius friction drag formula $-1.33/\sqrt{Re} = -0.03$ at $Re = 2000$.

$$F_\mu^* = \frac{1}{L} \oint \langle f_\mu^* \rangle dr, \quad (25)$$

is plotted as a function of the Strouhal number for the lowest and highest pitching angle considered, that is 5° and 15° , respectively, for a pitch-pivot point at the leading edge ($q = 0$). We observe that the drag is systematically larger (in magnitude) for the smallest angle, i.e., when the reduced frequency at a given Strouhal number is higher, according to relation (16). Fig. 14 also shows the Blasius friction drag formula $-1.33/\sqrt{Re}$ often used in the literature to estimate the laminar, skin friction of a slender body oscillating in a uniform flow; see for instance the experimental results reported in [62,63] for Reynolds numbers in the range from 10^3 to 10^4 , similar to those considered herein. For $Re = 2000$, the Blasius formula gives a viscous drag of -0.03 , which is consistent with the values ranging from -0.02 to -0.04 obtained for $\alpha_0 = 15^\circ$. Conversely, the results obtained for $\alpha_0 = 5^\circ$ departs increasingly and significantly from the Blasius prediction as St increases, up to 150% at $St = 0.5$.

For the lowest Strouhal number $St = 0.2$, it can be seen in Fig. 15(a) that the viscous stress distribution does approximately follow the Blasius law $-0.33/\sqrt{Re} r/L$ shown as the black-dotted line (the singular point $r = 0$ being omitted), if one excepts the regions near the leading and trailing edges. The steep slope near $r = 0$ in the values for both angles is the mark of the singularity at the leading edge. The discrepancy with the Blasius prediction in the rear part of the plate is due to the fact that the flow accelerates on average as it approaches the

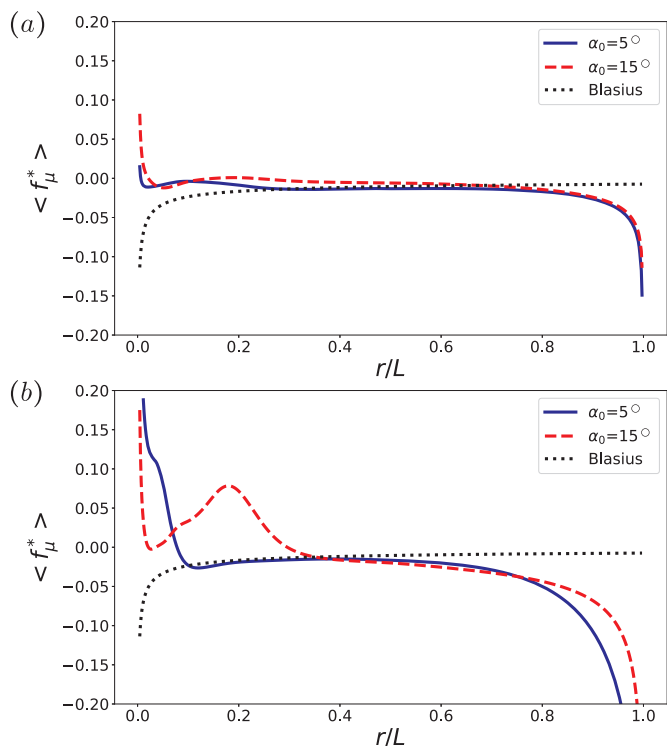


Fig. 15. Dimensionless mean viscous stress $\langle f_\mu^* \rangle$ computed along the plate’s upper face as function of the distance r/L from the leading edge for (a) $St = 0.2$ and (b) $St = 0.5$. For both figures, the curves for the angles $\alpha_0 = 5^\circ$ (—) and $\alpha_0 = 15^\circ$ (- -) are shown. The pitch-pivot point is at the leading edge ($q = 0$), the Reynolds number is $Re = 2000$. The Blasius formula $-0.33/\sqrt{Re(r/L)}$ is shown as well as the dotted line.

trailing edge and $\langle f_\mu^* \rangle$ increases accordingly (in magnitude). This effect however becomes larger with the pitching frequency, as seen in Fig. 15(b) for the Strouhal number $St = 0.5$, and it is especially steep for $\alpha_0 = 5^\circ$ (note that for a better comparison between the results for both Strouhal numbers, Fig. 15(b) is cut at the lowest value $\langle f_\mu^* \rangle = -0.2$, even though the skin friction still continues to decrease when r/L approaches 1). This likely explains why the Blasius estimate of the viscous drag force is off by a factor of almost 3. The viscous stress distribution for $\alpha_0 = 15^\circ$ at the high pitching frequency is more complex, because of the averaged flow field separation occurring at the leading edge. The latter is visible in Fig. 15(b) from the positive stress values in the range $0 < r/L < 0.3$, and somehow compensates the increase in the trailing-edge friction. This explains the relative agreement with the Blasius value seen in Fig. 14 for this pitching frequency. However, the intensity of the separation along oscillating boundaries can hardly be generally estimated. Note, that as shown in [64], the viscous drag even for vanishing frequencies depends on the pitching angle. Blasius scaling laws hence hardly provide reliable drag scaling for large span-to-chord aspect ratio flapping plates (the present two-dimensional configuration being a limit case). This is even more true for plates with small aspect ratios, whose skin friction is considerably modified by the oscillating boundary (with regard to a motionless plate). This has been put forward by the Bones-Lighthill boundary-layer thinning hypothesis [65], and further rationalized in [66].

CRediT authorship contribution statement

J er mie Labasse: Software, Investigation, Visualization, Formal analysis, Writing - original draft. **Uwe Ehrenstein:** Conceptualization, Methodology, Writing - original draft, Writing - review & editing. **Philippe Meliga:** Writing - original draft, Conceptualization, Methodology.

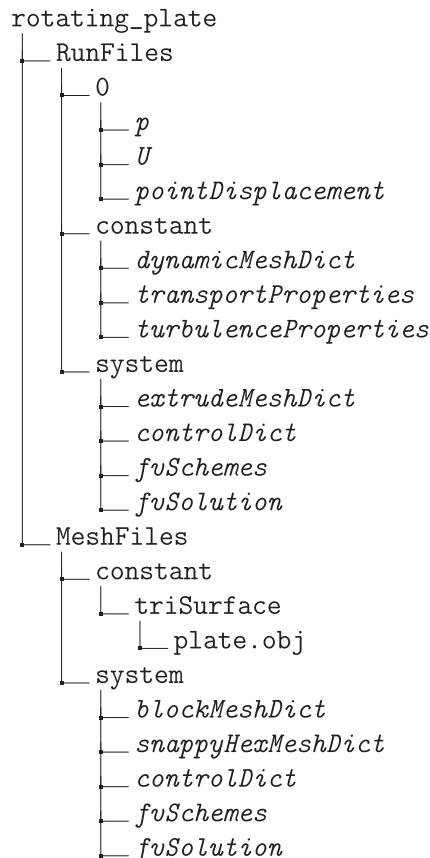
Declaration of Competing Interest

The authors declare that they have no known competing financial interests or personal relationships that could have appeared to influence the work reported in this paper.

Acknowledgment

Centre de Calcul Intensif d’Aix-Marseille is acknowledged for granting access to its high performance computing resources.

Appendix A. OpenFOAM dynamic mesh dictionary



This Appendix aimed at the OpenFOAM users community describes the various steps needed to use the build-in Laplacian-based dynamic mesh support. The reader interested in further technical details is referred to [44,45]. The file structure of a classical OpenFOAM set-up is reproduced above. The mesh is created in the **MeshFiles** directory, and the files *controlDict*, *fvSchemes* and *fvSolution* are systems files, specifying respectively the run control parameters, discretization schemes and equation solvers. The *blockMeshDict* is the file where the domain and the patch names are created, and the *snappyHexMeshDict* refines the domain and “snaps” the object geometry given by an.obj file (here the plate, created with the software *Blender* [67]). Boundary layer zones can be defined in the vicinity of the plate for further mesh refinements. Once the geometry and the mesh have been created, they must be imported in the **runFiles** directory with the help of the *extrudeMeshDict* file. The initial and boundary conditions for the velocity and the pressure are set in the *U* and *p* files. In the *transportProperties* the kinematic viscosity is set and in the *turbulenceProperties* file the simulation type must be specified (here “laminar”). The *pointVectorField* class and the *displacementLaplacian* solver are included in the dictionary file *dynamicMeshDict* with the diffusivity model (*inverseDistance* in our case). The type of the object motion is chosen in *pointDisplacement*, here

References

[1] <https://openfoam.org/version/6/>, 2018.

[2] W.J. McCroskey, Unsteady airfoils, *Annu. Rev. Fluid. Mech.* 14 (1982) 285–311, <https://doi.org/10.1146/annurev.fl.14.010182.001441>.

[3] R. Godoy-Diana, B. Thiria, On the diverse roles of fluid dynamic drag in animal swimming and flying, *J. R. Soc. Interface* 15 (2018) 20170715, <https://doi.org/10.1098/rsif.2017.0715>.

[4] T. Von Kármán, J. Burgers, *Aerodynamic Theory: General Aerodynamic Theory: Perfect Fluids* / [By] Th. von Kármán; J. M. Burgers, vol. 2, J. Springer, 1943.

[5] M.M. Koochesfahani, Vortical patterns in the wake of an oscillating airfoil, *AIAA J.* 27 (1989) 1200–1205, <https://doi.org/10.2514/3.10246>.

[6] D.G. Bohl, M.M. Koochesfahani, MTV measurements of the vortical field in the wake of an airfoil oscillating at high reduced frequency, *J. Fluid Mech.* 620 (2009) 63–88, <https://doi.org/10.1017/S0022112008004734>.

[7] J. Moubogha Moubogha, U. Ehrenstein, J.A. Astolfi, Forces on a pitching plate: an experimental and numerical study, *Appl. Ocean Res.* 69 (2017) 27–37, <https://doi.org/10.1016/j.apor.2017.09.003>.

[8] J.M. Anderson, K. Streitlien, D.S. Barrett, M.S. Triantafyllou, Oscillating foils of high propulsive efficiency, *J. Fluid Mech.* 360 (1998) 41–72, <https://doi.org/10.1017/S0022112097008392>.

[9] D.A. Read, F.S. Hover, M.S. Triantafyllou, Forces on oscillating foils for propulsion and maneuvering, *J. Fluids Struct.* 17 (2003) 163–183, [https://doi.org/10.1016/S0889-9746\(02\)00115-9](https://doi.org/10.1016/S0889-9746(02)00115-9).

[10] A.W. Mackowski, C.H.K. Williamson, Effect of pivot location and passive heave on propulsion from a pitching airfoil, *Phys. Rev. Fluids* 2 (2017) 013101, <https://doi.org/10.1103/PhysRevFluids.2.013101>.

[11] D. Floryan, T. Van Buren, C.W. Rowley, A.J. Smits, Scaling the propulsive performance of heaving and pitching foils, *J. Fluid Mech.* 822 (2017) 386–397, <https://doi.org/10.1017/jfm.2017.302>.

[12] M.S. Triantafyllou, F.S. Hover, A.H. Techet, D.K. Yue, Review of hydrodynamic scaling laws in aquatic locomotion and fishlike swimming, *Appl. Mech. Rev.* 58 (2005) 226–237, <https://doi.org/10.1115/1.1943433>.

[13] G.S. Triantafyllou, M. Triantafyllou, M. Grosenbaugh, Optimal thrust development in oscillating foils with application to fish propulsion, *J. Fluids Struct.* 7 (2) (1993) 205–224, <https://doi.org/10.1006/jfls.1993.1012>.

[14] K.D. Jones, M. Platzer, Numerical computation of flapping-wing propulsion and power extraction, 35th AIAA Aerospace Sciences Meeting, AIAA Paper 97–0826, 1997.

[15] Z. Yu, C. Eloy, Extension of Lighthill’s slender-body theory to moderate aspect ratios, *J. Fluids Struct.* 76 (2018) 84–94, <https://doi.org/10.1016/j.jfluidstructs.2017.09.010>.

[16] K. Moored, D. Quinn, Inviscid scaling laws of a self-propelled pitching airfoil, *AIAA J.* 57 (2019) 3686–3700, <https://doi.org/10.2514/1.J056634>.

[17] F. Ayancik, Q. Zhong, D. Quinn, A. Brandes, H. Bart-Smith, K. Moored, Scaling laws for the propulsive performance of three-dimensional pitching propulsors, *J. Fluid Mech.* 871 (2019) 1117–1138, <https://doi.org/10.1017/jfm.2019.334>.

[18] A. Andersen, T. Bohr, T. Schnipper, J.H. Walther, Wake structure and thrust generation of a flapping foil in two-dimensional flow, *J. Fluid Mech.* 812 (2017) R4, <https://doi.org/10.1017/jfm.2016.808>.

[19] X. Wu, X. Zhang, X. Tian, X. Li, W. Lu, A review on fluid dynamics of flapping foils, *Ocean Eng.* 195 (2020) 1–30, <https://doi.org/10.1016/j.oceaneng.2019.106712>.

[20] R. Ramamurti, V. Sandberg, Simulation of flow about flapping airfoils using finite element incompressible flow solver, *AIAA J.* 39 (2001) 253–260, <https://doi.org/10.2514/2.1320>.

[21] U. Ehrenstein, Thrust and drag scaling of a rigid low-aspect-ratio pitching plate, *J. Fluids Struct.* 87 (2019) 39–57, <https://doi.org/10.1016/j.jfluidstructs.2019.03.013>.

[22] C.S. Peskin, Flow patterns around heart valves: a numerical method, *J. Comput. Phys.* 10 (1972) 252–271, [https://doi.org/10.1016/0021-9991\(72\)90065-4](https://doi.org/10.1016/0021-9991(72)90065-4).

[23] A. Pinelli, I.Z. Naqvi, U. Piomelli, J. Favier, Immersed-boundary methods for general finite-difference and finite-volume Navier-Stokes solvers, *J. Comp. Phys.* 229 (2010) 9073–9091, <https://doi.org/10.1016/j.cp.2010.08.021>.

[24] B. Kallemov, A. Bhalla, B.E. Griffith, A. Donev, An immersed boundary method for rigid bodies, *Comm. Appl. Math. Comput. Sci.* 11 (2016) 79–141, <https://doi.org/10.2140/camcos.2016.11.79>.

[25] A. Goza, T. Colonius, A strongly-coupled immersed-boundary formulation for thin elastic structures, *J. Comp. Phys.* 336 (2017) 401–411, <https://doi.org/10.1016/j.cp.2017.02.027>.

[26] P. Das, Comparison of a priori and a posteriori meshes for singularly perturbed nonlinear parameterized problems, *J. Comput. Appl. Math.* 290 (2015) 16–25, <https://doi.org/10.1016/j.cam.2015.04.034>.

[27] P. Das, S. Rana, J. Vigo-Aguiar, Higher order accurate approximations on equidistributed meshes for boundary layer originated mixed type reaction diffusion systems with multiple scale nature, *Appl. Numer. Math.* 148 (2020) 79–97, <https://doi.org/10.1016/j.apnum.2019.08.028>.

[28] P. Bar-Yoseph, S. Mereu, S. Chippada, V. Kalro, Automatic monitoring of element shape quality in 2-d and 3-d computational mesh dynamics, *Comput. Mech.* 27 (2001) 378–395, <https://doi.org/10.1007/s004660100250>.

[29] J. Batina, Unsteady euler airfoil solutions using unstructured dynamic meshes, *AIAA J.* 28 (1990) 1381–1388, <https://doi.org/10.2514/6.1989-115>.

[30] C. Farhat, C. Degand, B. Koobus, Lesoinne, Torsional springs for two-dimensional dynamic unstructured fluid meshes, *Comput. Methods Appl. Mech. Eng.* 163 (1998) 231–245, [https://doi.org/10.1016/S0045-7825\(98\)00016-4](https://doi.org/10.1016/S0045-7825(98)00016-4).

[31] F.J. Blom, Considerations on the spring analog, *Int. J. Num. Meth. Fluids* 32 (2000) 647–668, [https://doi.org/10.1002/\(SICI\)1097-0363\(20000330\)32:6<647::AID-FLD979>3.0.CO;2-K](https://doi.org/10.1002/(SICI)1097-0363(20000330)32:6<647::AID-FLD979>3.0.CO;2-K).

[32] A. Johnson, T. Tezduyar, Mesh update strategies in parallel finite element computations of flow problems with moving boundaries and interfaces, *Comput. Methods Appl. Mech. Eng.* 119 (1994) 73–94, [https://doi.org/10.1016/0045-7825\(94\)00077-8](https://doi.org/10.1016/0045-7825(94)00077-8).

[33] K. Stein, T. Tezduyar, R. Benny, Mesh moving techniques for fluid-structure interactions with large displacements, *J. Appl. Mech.* 70 (2003) 58–63, <https://doi.org/10.1115/1.1530635>.

[34] R. Löhner, C. Yang, Improved ale mesh velocities for moving bodies, *Comm. Numer. Meth. Eng.* 12 (1996) 599–608, [https://doi.org/10.1002/\(SICI\)1099-0887\(199610\)12:10<599::AID-CNMI>3.0.CO;2-Q](https://doi.org/10.1002/(SICI)1099-0887(199610)12:10<599::AID-CNMI>3.0.CO;2-Q).

[35] D. Littlefield, The use of r-adaptivity with local, intermittent remesh for modeling hypervelocity impact and penetration, *Int. J. Impact Engrg.* 26 (2001) 433–442, [https://doi.org/10.1016/S0734-743X\(01\)00093-8](https://doi.org/10.1016/S0734-743X(01)00093-8).

[36] G.R. Tabor, M.H. Baba-Ahmadi, Inlet conditions for large eddy simulation: a review, *Comp. Fluids* 39 (2010) 553–567, <https://doi.org/10.1016/j.compfluid.2009.10.007>.

[37] M. Meldi, M.V. Salvetti, P. Sagaut, Quantification of errors in large-eddy simulations of a spatially evolving mixing layer using polynomial chaos, *Phys. Fluids* 24 (2012) 035101, <https://doi.org/10.1063/1.3688135>.

[38] D.A. Lysenko, I.S. Ertesvåg, K.E. Rian, Modeling of turbulent separated flows using OpenFOAM, *Comp. Fluids* 80 (2013) 408–422, <https://doi.org/10.1016/j.compfluid.2012.01.015>.

[39] E. Constant, J. Favier, M. Meldi, P. Meliga, E. Serre, An immersed boundary method in OpenFOAM: verification and validation, *Comput. Fluids* 157 (2017) 52–72, <https://doi.org/10.1016/j.compfluid.2017.08.001>.

[40] P. Meliga, E. Boujo, M. Meldi, F. Gallaire, Revisiting the drag reduction problem using adjoint-based distributed forcing of laminar and turbulent flows over a circular cylinder, *Eur. J. Mech. B Fluid* 72 (2018) 123–134, <https://doi.org/10.1016/j.euromechflu.2018.03.009>.

[41] L. Gao, J. Xu, G. Gao, Numerical simulation of turbulent flow past airfoils on OpenFOAM, *Procedia Eng.* 31 (2012) 756–761, <https://doi.org/10.1016/j.proeng.2012.01.1098>.

[42] F. Flores, R. Garreaud, R.C. Muñoz, CFD simulations of turbulent buoyant atmospheric flows over complex geometry: solver development in OpenFOAM, *Comp. Fluids* 82 (2013) 1–13, <https://doi.org/10.1016/j.compfluid.2013.04.029>.

[43] B. Selma, M. Désilets, P. Proulx, Optimization of an industrial heat exchanger using an open-source CFD code, *Appl. Therm. Eng.* 69 (2014) 241–250, <https://doi.org/10.1016/j.applthermaleng.2013.11.054>.

[44] H. Jasak, Dynamic mesh handling in OpenFOAM, 47th AIAA Aerospace Science Meeting, 5–8 January 2009, Orlando, Florida, (2009).

[45] H. Jasak, Z. Tuković, Dynamic mesh handling in OpenFOAM applied to fluid-structure interaction simulations, in: J. Pereira, A. Sequeira (Eds.), *ECCOMAS CFD 2010*, Lisbon, Portugal, 14–17 June 2010, 2010.

[46] J. Ferziger, M. Perić, *Computational Methods for Fluid Dynamics*, third ed., Springer, 2002.

[47] H. Schlichting, *Boundary-layer Theory*, McGraw-Hill, 1979.

[48] A.O. González, Mesh motion alternatives in OpenFOAM, <http://www.tfd.chalmers.se/~hani/kurser/OS-CFD-2009/AndreuOliverGonzalez/ProjectReport-Corrected.pdf>, (2009).

[49] F.M. Bos, *Numerical Simulations of Flapping Foil and Wing Aerodynamics*, Delft University of Technology, 2009 Ph.D. thesis.

[50] S. Lele, Compact finite difference schemes with spectral-like resolution, *J. Comp. Phys.* 103 (1992) 16–42, [https://doi.org/10.1016/0021-9991\(92\)90324-R](https://doi.org/10.1016/0021-9991(92)90324-R).

[51] I. Solak, *Direct Numerical Simulation and Large Scale Analysis of a Turbulent Boundary Layer*, Université de Lille, 2018 Ph.D. thesis.

[52] P. Das, A higher order difference method for singularly perturbed parabolic partial differential equations, *J. Differ. Equ. Appl.* 24 (2018) 452–477, <https://doi.org/10.1080/10236198.2017.1420792>.

[53] T.Y. Wu, Swimming of a waving plate, *J. Fluid Mech.* 10 (1961) 321–344, <https://doi.org/10.1017/S0022112061000949>.

[54] Y. Yadykin, V. Tenetov, D. Levin, The added mass of a flexible plate oscillating in a fluid, *J. Fluids Struct.* 17 (2003) 115–123, [https://doi.org/10.1016/S0889-9746\(02\)00100-7](https://doi.org/10.1016/S0889-9746(02)00100-7).

[55] S. Ramanarivo, R. Godoy-Diana, B. Thiria, Passive elastic mechanism to mimic fish-muscle action in anguilliform swimming, *J. R. Soc. Interface* 10 (2013) 20130667, <https://doi.org/10.1098/rsif.2013.0667>.

[56] M. Píneiru, R. Godoy-Diana, B. Thiria, Resistive thrust production can be as crucial as added mass mechanisms for inertial undulatory swimmers, *Phys. Rev. E* 92 (2015) 021001(R), <https://doi.org/10.1103/PhysRevE.92.021001>.

[57] P. Payne, The virtual mass of a rectangular flat plate of finite aspect ratio, *Ocean Eng.* 8 (1981) 541–545, [https://doi.org/10.1016/0029-8018\(81\)90018-4](https://doi.org/10.1016/0029-8018(81)90018-4).

[58] M. Saadat, F.E. Fish, A.G. Domel, V. Di Santo, G. Lauder, H. Haj-Hariri, On the rules for aquatic locomotion, *Phys. Rev. Fluids* 2 (2017) 083102, <https://doi.org/10.1103/PhysRevFluids.2.083102>.

[59] W. Tian, A. Bodling, H. Liu, J.C. Wu, G. He, H. Hu, An experimental study of the effects of pitch-pivot-point location on the propulsion performance of a pitching airfoil, *J. Fluids Struct.* 60 (2016) 130–142, <https://doi.org/10.1016/j.jfluidstructs.2015.10.014>.

[60] I.E. Garrick, *Propulsion of a Flapping and Oscillating Airfoil*, Langley Memorial Aeronautical Lab. Rept. 567, Langley Field, VA, 1936.

[61] T. Theodorson, *General Theory of Aerodynamic Instability and the Mechanism of Flutter*, NACA TR 498, 1935.

- [62] S. Alben, C. Witt, T. Baker, E. Anderson, G. Lauder, Dynamics of freely swimming flexible foils, *Phys. Fluids* 24 (2012) 051901, <https://doi.org/10.1063/1.4709477>.
- [63] V. Raspa, S. Ramananarivo, B. Thiria, R. Godoy-Diana, Vortex-induced drag and the role of aspect ratio in undulatory swimmers, *Phys. Fluids* 26 (2014) 041701, <https://doi.org/10.1063/1.4870254>.
- [64] A.W. Mackowski, C.H.K. Williamson, Direct measurement of thrust and efficiency of an airfoil undergoing pure pitching, *J. Fluid Mech.* 765 (2015) 524–543, <https://doi.org/10.1017/jfm.2014.748>.
- [65] M.J. Lighthill, Large-amplitude elongated-body theory of fish locomotion, *Proc. R. Soc. Lond. B* 179 (1971) 125–138, <https://doi.org/10.1098/rspb.1971.0085>.
- [66] U. Ehrenstein, C. Eloy, Skin friction on a moving wall and its implications for swimming animals, *J. Fluid Mech.* 718 (2013) 321–346, <https://doi.org/10.1017/jfm.2012.613>.
- [67] (2017). <https://blender.org/download/releases/2-79/>